Clay Minerals (2024), **59**, 298–309
doi:10.1180/clm.2024.19

CAMBRIDGE UNIVERSITY PRESS

Article

The acid-leaching process and structural changes of lizardite, chlorite and talc in sulfuric acid medium

Dingran Zhao[1,2], Hongjuan Sun[1,2], Tongjiang Peng[1,2], Li Zeng[1,2] and Mengji Wu[1,2]

[1]Key Laboratory of Ministry of Education for Solid Waste Treatment and Resource Recycle, Southwest University of Science and Technology, Mianyang, Sichuan, China and [2]Institute of Mineral Materials and Applications, Southwest University of Science and Technology, Mianyang, Sichuan, China

Abstract

Trioctahedral phyllosilicate minerals are widely distributed on the Earth's surface, especially in soil. The mineral–water interfacial reaction of lizardite, chlorite and talc, with various structural properties (tetrahedral sheet, octahedral sheet, 1:1-type and 2:1-type interlayer domain/two-dimensional structural units), was carried out in sulfuric acid solution (1 mol L^{-1}). The mineral samples were characterized by powder X-ray diffraction, Fourier-transform infrared spectroscopy, scanning and transmission electron microscopy and inductively coupled plasma mass spectrometry. The dissolution concentration, dissolution rate, dissolution rules and structural changes of the components during the dissolution processes of the various two-dimensional structural units were studied. The results show that the dissolution concentrations of Si and Mg in the sulfuric acid solution decrease in the following order: chlorite > lizardite > talc and lizardite > chlorite > talc. The dissolution rates of Si in chlorite and Mg in lizardite are the greatest, while talc is the most stable compared with lizardite and chlorite. With increasing interfacial reaction time and the dissolution of the ionic components of the minerals, the structure of lizardite is gradually destroyed; the structural destruction of chlorite is more obvious during the early stages of the reaction; and the structure of talc does not significantly change over the course of the entire reaction. By analysing the microtopography of the minerals, it was found that the structural failure of lizardite occurred from the surface to the interior. Chlorite had more structural defects and showed collapse of the layered structure during structural failure. The surface layer of talc decomposed by corrosion into a small lamellae structure attached to the surface, but there was no obvious structural change similar to those of lizardite and chlorite. The relationship between the evolution of composition and structure during the mineral–water interfacial reaction process with the two-dimensional structure layer type provides the mineralogical basis for studying the coupling mechanism of the migration and transformation of materials in key regions of the Earth.

Keywords: Chlorite; ionic dissolution; lizardite; mineral–water interfacial reactions; structural changes; talc

(Received 6 May 2024; revised 12 July 2024; accepted 29 July 2024)

Trioctahedral phyllosilicate minerals (TPSMs) can be broadly divided into minerals such as lizardite, talc, phlogopite, vermiculite and chlorite. The structural layer of a TPSM is composed of tetrahedral (Si_4O_{10}) and octahedral Mg–(O,OH) sheets stacked in various ways (Hegyesi *et al.*, 2020). On the Earth's surface, TPSMs constantly undergo physical or chemical processes, such as mineral dissolution, ion exchange/adsorption and structural evolution in aqueous solution, which are vital for maintaining the function of the Earth's ecosystems (Hao *et al.*, 2019; Zhu *et al.*, 2021, 2023; Gao *et al.*, 2023). Mineral–water interfacial reactions involve almost all geochemical processes, including crystallization, alteration, weathering and the formation of clay minerals. In these geological processes, with the help of the 'water' medium, the chemical components of minerals are either dissolved, migrated and enriched or residually fixed. The surface water on the Earth is not pure water as the soil is slightly acidic due to the reproduction and growth of plants, microorganisms and animals (Palmieri *et al.*, 2019; Ren *et al.*, 2023). Thus, mineral–water interfacial reactions occurring in acidic media lead to greater reaction rates and increased reaction complexity.

The mineral–water interfacial reactions of TPSMs have attracted extensive attention in the study of acid-leaching and acid-etching mechanisms. Studies show that upon the acid treatment of antigorite, chrysotile and lizardite, Mg^{2+} in serpentine minerals has differential dissolution characteristics, and the extraction efficiency of Mg^{2+} is closely related to the crystal structure, chemical properties and microscopic morphology of these minerals (Lacinska *et al.*, 2016). In vermiculite, Mg^{2+} is preferentially dissolved, and other metal ions do not interfere in the process. However, Al^{3+} in the tetrahedral sheet has a greater dissolution rate at the initial stage and is readsorbed to the interlayer domain to form hydroxy-aluminium interlayer minerals over time (Kalinowski & Schweda, 2007). After chrysotile has been treated with acid, the specific surface area, maximum adsorption capacity and pore volume of the chrysotile increased with increasing dissolution rate. The hydroxyl group and Mg^{2+} were removed in sequence in the octahedral sheets, and the residual Si–O tetrahedral sheets were reconstructed (Bo *et al.*, 2013). Another study showed that when chlorite reacts with a

Corresponding author: Hongjuan Sun; Email: sunhongjuan@swust.edu.cn

Cite this article: Zhao D, Sun H, Peng T, Zeng L and Wu M (2024) The acid-leaching process and structural changes of lizardite, chlorite and talc in sulfuric acid medium. *Clay Minerals* **59**, 298–309. https://doi.org/10.1180/clm.2024.19

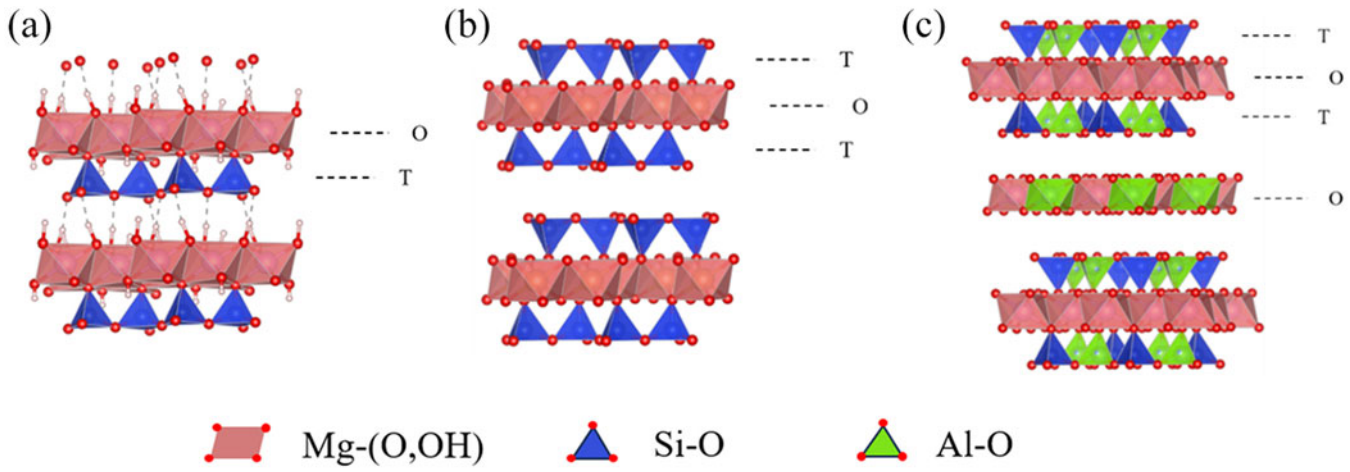

Figure 1. Schematic diagram of the crystal structures of (a) lizardite, (b) talc and (c) chlorite.

solution with pH values ranging from 2 to 6, the pH influences the dissolution rate of chlorite and the sequence of ion release; additionally, at higher concentrations of H^+, the preferential release of Fe^{3+} from the octahedral sheet is favourable (Liao *et al.*, 2021). The dissolution acid-etching process and dissolving mechanism of TPSM are different from those of typical minerals with no obvious anisotropy in their chemical bonds such as calcite minerals (Ruiz-Agudo & Putnis, 2012; Urosevic *et al.*, 2012; Li *et al.*, 2020). The dissolution or acid corrosion process of calcite minerals was found to be approximately uniform from the surface to the interior. However, dissolution does not occur uniformly on all exposed surfaces during TPSM weathering; rather, it occurs preferentially at some locations with weak structures or excess surface energy, such as at dislocations, vacancies and sub-grain boundaries. Cavitation microbubbles in the fluid can accelerate the dissolution of mineral crystals (Su & Zhou, 2019).

In acidic media, the dissolution process of minerals, which can include changes in composition and structure, is mainly controlled by the structure of the minerals and the properties of the reaction solution. The degree of difficulty of dissolution and structural adjustment of components in various two-dimensional structural units of the mineral structure can be determined from the properties of the metal cations and the strength of chemical bonds at structural positions. Typically, the degree of difficulty of dissolution decreases in the following order: tetrahedral sheet > octahedral sheet > interlayer space (Bo *et al.*, 2013). In addition, since the Si–O bond in the tetrahedral sheets is stronger than the Mg–(O,OH) bond in the octahedral sheets, the main processes in acidic media include the breaking of the interlayer and Mg–(O,OH) bonds (He *et al.*, 2019), the dissolution of components and the adjustment of the residual silica tetrahedral sheet skeleton. Therefore, a large number of studies have been conducted on the early stages on mineral–water interface interactions, mineral component dissolution processes and structural changes. However, comparative studies on the TPSM crystal structure (i.e. the layer-type differences) are relatively lacking.

In this study, according to the combination ratio and mode of the structural unit layers, lizardite (1:1 type, no interlayer; Fig. 1a), talc (2:1 type, no interlayer; Fig. 1b) and chlorite (2:1 type, (hydr)oxide interlayer; Fig. 1c), with obvious structural differences, were selected for conducting water–interface reactions in a sulfuric acid medium (Cuadros & Dudek, 2006; Gazze *et al.*, 2014; He *et al.*, 2016). TPSMs, with their differing structural layers, have various compositions, structural properties and chemical bond strengths. Thus, they have varying thermodynamic and chemical stabilities, and the siloxane and hydroxyl base planes and the corresponding edges (end faces) formed by them should have varying chemical activities. The aim of this work is to understand the dissolution mechanism during the mineral–water interfacial reaction through the examination of the dissolution rate of structurally varying minerals in an acid aqueous solution system. The various dissolution processes of the chemical components and the structural evolution of the various structural layers during the mineral–water interfacial reaction are revealed, providing the crystal chemical basis for the study of mineral evolution such as the migration and transformation of the Earth's key regional substances and their mechanisms of action.

Materials and methods

Raw materials

The lizardite and chlorite samples were obtained from the Beiwagou Cuiyu jade mine, Xiuyan County, Liaoning Province, China. The talc sample was obtained from Guilin City, Guangxi Province, China. The samples were crushed, ground, passed through a 200 mesh sieve and ultrasonically rinsed three times with ultrapure water to minimize the effects of the high-energy surface sites and fine particles produced, and they were analysed using X-ray diffraction (XRD).

Experimental procedure

At 25°C, 1 g each of lizardite, chlorite and talc was placed in a 150 mL conical flask. A total of 100 mL of a 1.0 mol L^{-1} sulfuric acid solution was added to a volumetric flask at a solid-to-liquid ratio of 1:100. The acid concentration is designed for 1 mol L^{-1}. This can accelerate the process of mineral–water interfacial reaction and can help the mineral to fully react in the acid solution. It also provides sufficient H^+ to prevent experimental errors due to the dramatically smaller H^+ concentrations in the later stages of mineral–water interface reactions. The reaction times studied were 1, 2, 4, 12, 24, 72, 120, 168 and 216 h. The conical flask was placed in a constant-temperature shaker and the reaction was allowed to

https://doi.org/10.1180/clm.2024.19 Published online by Cambridge University Press

proceed fully. The reaction suspension was filtered to obtain the solid product and washed three times with distilled water until the pH of the filtrate was neutral. The solid product was dried in an oven at 60°C and set aside in a desiccator. The filtrate was collected in a 50 mL volumetric flask and left for subsequent inductively coupled plasma mass spectrometry testing. The samples were labelled as *K-T*, where *K* is the mineral sample number (i.e. Lz, Chl and Tlc, for lizardite, chlorite and talc, respectively) and *T* was the reaction time.

Characterization methods

The specific surface areas of lizardite, chlorite and talc were measured using the Brunauer–Emmett–Teller (BET) method with five-point N_2 adsorption isotherms after degassing the samples for 60 min at 120°C using a McASAP 2460 (Norcross, GA, USA) instrument.

Chemical analysis of major elements was performed using X-ray fluorescence (XRF). The sample was ground to a particle size of <74 μm (200 mesh) and then dried at 105°C in an oven for 2 h. Subsequently, the sample was precisely weighed to 0.8 g and incinerated at 1000°C for 1 h until the sample attained a constant weight, from which the ash content of the sample could be calculated. The fused sample was blended with a uniform mixture of solvent: 8.00 g $Li_2B_4O_7$–$LiBO_2$ ($m(Li_2B_4O_7)$:$m(LiBO_2)$ = 67:33), transferred into a platinum crucible and supplemented with four drops of a LiBr solution at a concentration of 200 g L^{-1} as a releasing agent. Subsequently, the sample was subjected to a melting process at 1050°C, followed by controlled cooling to facilitate the formation of a glassy slab. Elements were analysed using a S4 Pioneer (Bruker) wavelength-dispersive XRF spectrometer equipped with X-ray tube with a Rh anode and a maximum voltage/current of 60 kV/150 mA. The fundamental parameter method using *SpectraPlus* software was used to quantify the elements.

XRD was used to determine the mineralogical changes in the samples before and after the mineral–water interfacial reaction. XRD data were obtained using a D/max-IIIA diffractometer manufactured by Rigaku (Japan). A copper target with a sum-tube voltage of 40 kV and a sum-tube current of 40 mA was accompanied by a DS1/2(°) slit system. The powdered samples were analysed between 3 and 80°2θ. The step size was 0.02°2θ and the scan rate was 2 s $step^{-1}$.

A Fourier-transform infrared (FTIR) spectrometer was used to determine the changes in the crystal chemistry of the samples before and after the mineral–water interfacial reaction. The FTIR spectra were measured using a Frontier spectrometer from Parkin Elmer Instruments (China) following the KBr pressed pellet technique. For this measurement, a 0.9 mg aliquot of the dried subsample was mixed with 80.0 mg of oven-dried, spectroscopic-grade KBr salt (refractive index 1.559, particle diameter 5–20 μm), and then the mixture was ground for 1 min. The mixture was then pressed in a die with 10 t of pressure applied for 1 min to form a disc or pellet. The spectra were measured at room temperature in a test range of 4000–400 cm^{-1} over 64 scans.

The cation (Si, Mg) content in solution was measured using an inductively coupled plasma emission spectrometer (ThermoiCAP 6500, Waltham, MA, USA). Prior to each analysis, the ICP was calibrated ($r^2 > 0.999$) *via* serial dilution of certified standards.

Scanning electron microscopy (SEM) was conducted to study the micromorphology of the samples using a ZEISS Supra 55 Sapphire (Jena, Germany) field emission scanning electron microscope. The samples were spread on conductive carbon tape and the surface was carbon-sprayed before being placed in the sample chamber, vacuumed and observed at an accelerating voltage of 30 kV.

Transmission electron microscopy (TEM) was conducted using an American-FEI-Talos F200S (OR, USA) microscope accelerated at 200 kV. The lizardite, chlorite and talc samples were sonicated and dispersed in ethanol for 10 min. Drops of the sample suspensions were placed on a 200 mesh carbon-coated Cu grid for at least 10 min before being transferred to the microscope for measurement.

The average rate of dissolution of each ion in the mineral was calculated as Equation 1:

$$r_i(\bar{t}) = \frac{C_i \times m_1}{t \times m_0 \times \mathrm{SSA} \times \eta_i} \quad (1)$$

where C_i is the concentration of solute *i* (Si, Mg, Fe; mmol kg^{-1}) in the sample recovered at time *t;* m_1 is the mass of the sample solution before sampling (in kg); *t* is the sample reaction time; m_0 is the initial mass of the mineral (in g); SSA (m^2 g^{-1}) is the specific surface area of the mineral; and η_i is the stoichiometric coefficient of element *i* in the mineral.

Results and discussion

The results of XRF spectroscopy analysis of the purified samples of lizardite, chlorite and talc are shown in Table 1. The typical structural layer of lizardite is 0.44 nm thick and consists of tetrahedral and octahedral sheets (Mellini, 1982; Grobéty, 2003; Palacios-Lidon *et al.*, 2010; Evans *et al.*, 2013). In the tetrahedral sheets, Si is replaced by Al and Fe, while in the octahedral sheets, Mg is replaced by Fe and a small amount of Cr, Ni and Ti (Caruso & Chernosky, 1979; Mellini & Zanazzi, 1987; Viti & Mellini, 1997; Fuchs *et al.*, 1998). Chlorite consists of a negatively charged tetrahedral–octahedral–tetrahedral (TOT) layer with a thickness of 0.66 nm and a positively charged interlayer octahedral sheet with a thickness of 0.22 nm (Brigatti *et al.*, 2013). In the tetrahedral sheet, Al replaces Si, and in the octahedral sheet, Al and Fe replace Mg, and small amounts of Cr and Mn occupy the octahedral sheets (Barnhisel & Bertsch, 1989). Talc contains a TOT sheet, where the tetrahedral sheet only contains Si and there is a small amount of Fe instead of Mg in the octahedral sheets (Perez Rodriguez *et al.*, 1985; Temuujin *et al.*, 2003). The ion positions and tetrahedral and octahedral sheets in chlorite and lizardite were the same as was assumed, which would not affect the chemical formula of lizardite. Cations with <0.001 fractional contents in the composition are not included in the crystal formula. The crystal formulas calculated from the chemical analysis data are as follows:

Lizardite: $(Mg_{5.418}Fe_{0.402}Cr_{0.028}Ni_{0.02}Ti_{0.007})_{5.875}(Si_{3.777}Al_{0.123}Fe_{0.1})_4O_{10}(OH)_8$

Chlorite: $(Mg_{3.401}Fe_{1.105}Al_{0.956}Mn_{0.033}Cr_{0.007})_{5.502}[(Si_{2.586}Al_{1.414})_4O_{10}](OH)_8$

Talc: $(Mg_{2.987}Fe_{0.013})_3(Si_4O_{10})(OH)_2$

Dissolution processes of Si and Mg at the lizardite–water, chlorite–water and talc–water interfaces in sulfuric acid solutions

Mineral–water interfacial reactions are related to the formation and transfer of charges, which occur when substances at the mineral surface break bonds with the lattice, forming ions and moving into the solution (Knauss & Wolery, 1988). The concentrations

https://doi.org/10.1180/clm.2024.19 Published online by Cambridge University Press

Table 1. Chemical compositions of lizardite (Lz), chlorite (Chl) and talc (Tlc) mineral samples (wt.%).

Sample	SiO_2	MgO	Fe_2O_3	Al_2O_3	K_2O	Cr_2O_3	BaO	NiO	SO_3	TiO_2	CaO	MnO	LOI	Sum
Lz	38.93	37.46	6.88	1.08	0.59	0.36	0.30	0.26	0.17	0.10	0.10	0.01	13.67	100.00
Chl	25.74	22.71	14.61	20.01	0.59	0.09	0.28	<0.01	0.11	4.48	0.42	0.39	10.44	100.00
Tlc	64.25	32.01	0.27	0.05	0.42	<0.01	0.20	<0.01	0.02	0.02	0.61	<0.01	2.03	100.00

LOI = loss on ignition.

Table 2. Elemental analysis of the liquid phase during the mineral–water interfacial reaction of lizardite (Lz), chlorite (Chl) and talc (Tlc; mg L^{-1}).

	Si			Mg			Fe		
Time (h)	Lz	Chl	Tlc	Lz	Chl	Tlc	Lz	Chl	Tlc
1	13.79	20.42	1.90	132.01	48.51	32.01	14.50	24.23	<0.01
2	19.30	28.03	2.22	189.82	65.58	38.82	20.13	27.37	<0.01
4	20.78	41.52	3.13	229.62	95.71	41.39	23.64	31.01	<0.01
12	38.72	51.82	4.68	574.08	105.52	46.18	53.32	45.45	<0.01
24	46.82	55.24	7.59	780.82	116.09	50.91	72.21	57.79	<0.01
72	52.02	82.21	14.52	1186.78	129.02	59.02	115.94	95.19	<0.01
120	60.64	104.56	17.79	1353.79	136.18	61.13	135.38	114.91	<0.01
168	57.21	114.19	23.01	1667.41	144.41	75.52	146.36	139.70	<0.01
216	54.86	128.69	23.72	1719.22	162.52	73.88	153.26	141.06	<0.01

of Mg, Si and Fe in the collected filtrate were analysed and calculated (Table 2), and the dissolution concentrations of Mg, Si and Fe in Lz, Chl and Tlc were obtained. When chlorite and talc react with the sulfuric acid solution, the Si concentration in the filtrate increases and the Si concentration in chlorite and talc slightly increases (Fig. 2a). However, the Si concentration in the filtrate reaches a peak and then slowly decreases after the reaction of lizardite for 120 h (Fig. 2a). This can be attributed to the reaction of H^+ with $(OH)^-$ and $[SO_4]^{2-}$ with Mg^{2+} in the solution after the reaction of lizardite in the sulfuric acid medium for 120 h. This results in the reduction of the acid concentration in the solution, the formation of amorphous silica and the precipitation of metasilicic acid in the solution.

The Si dissolution concentration decreases in the following order: chlorite > lizardite > talc (Fig. 2a). The Si dissolution concentration in chlorite is the greatest, which can be attributed to the Al substitution of Si in the silica tetrahedral sheet of chlorite and preferential dissolution of Al from the silica tetrahedral sheet compared to Si (Table 3; Hamer *et al.*, 2003). This leads to more structural defects, resulting in Si being connected to the mineral surface by fewer than three bridging oxygenates. The Si can detach from the octahedral sheet faster (Saldi *et al.*, 2007; Galí *et al.*, 2012), resulting in the Si in chlorite dissolving more easily than that in lizardite and talc. Additionally, the dissolution concentration of Si in lizardite is greater than that of talc because the silica tetrahedral sheet in lizardite has small amounts of Al and Fe instead of Si. By contrast, the silica tetrahedral sheet in talc has almost no Al and Fe and there are few defect sites. Therefore, the dissolution concentration of Si in talc is the lowest during the mineral–water interfacial reaction in acidic medium.

The Mg dissolution concentration decreases in the following order: lizardite > chlorite > talc (Fig. 2b). The difference in the dissolution concentration of Mg is mainly due to the varying structures of the minerals. Lizardite is the 1:1-type mineral, while talc and chlorite are 2:1-type minerals. When H^+ in the sulfuric acid solution enters the interlayer domain of lizardite, Mg–OH on each octahedral sheet reacts fully with H^+, and a great amount of Mg is released from the octahedral sheet. Furthermore, when H^+ attacks $(OH)^-$ on the octahedral sheet by the mineral edge (end face) of chlorite and talc, the outer octahedral sheet is destroyed and a small amount of Mg is dissolved. During the talc–water interfacial reaction, the dissolution of Mg gradually occurs from the outside to the inside at the mineral edge (end face). Due to the dissolution of Mg, the silica tetrahedral sheet on both sides gradually collapses into the middle, resulting in the dissolution of Mg from Mg–OH into the solution (Okada *et al.*, 2003). Therefore, the dissolution concentration of Mg in the 2:1-type mineral is lower than that in the 1:1-type mineral.

The Fe dissolution concentration decreases in the following order: lizardite > chlorite (Fig. 2c). The dissolved concentration of Fe in talc is lower than the detection limit of the ICP test and can be ignored. Fe in chlorite exists only in octahedral sheets. Therefore, the dissolution pattern of Fe in chlorite is similar to that of Mg. However, compared to Fe, Mg is more soluble in lizardite and chlorite, and Mg is preferentially dissolved. This phenomenon is associated with ionic polarization and bond strength (Heller-Kallai & Rozenson, 1981; He *et al.*, 2002). When Mg and Fe adopt an octahedral coordination with oxygen, the cation's ability to polarize affects the ionic bond strength. The ionic radii of Fe and Mg are 0.055 and 0.072 nm, respectively, indicating that the order of polarization ability is Fe > Mg; thus, the resulting ionic bond strength with oxygen follows the order Fe–O > Mg–O.

In minerals, the macroscopic dissolution rate of ions is typically related to the normalization of the specific surface area of reaction. Various reaction-specific surface area models have been proposed for different minerals: (1) the reaction-specific surface area is usually assumed to be the BET specific surface area of the mineral or proportional to the BET surface area (Ganor *et al.*, 1999; Villanova-de-Benavent *et al.*, 2022); or (2) the reaction-specific

https://doi.org/10.1180/clm.2024.19 Published online by Cambridge University Press

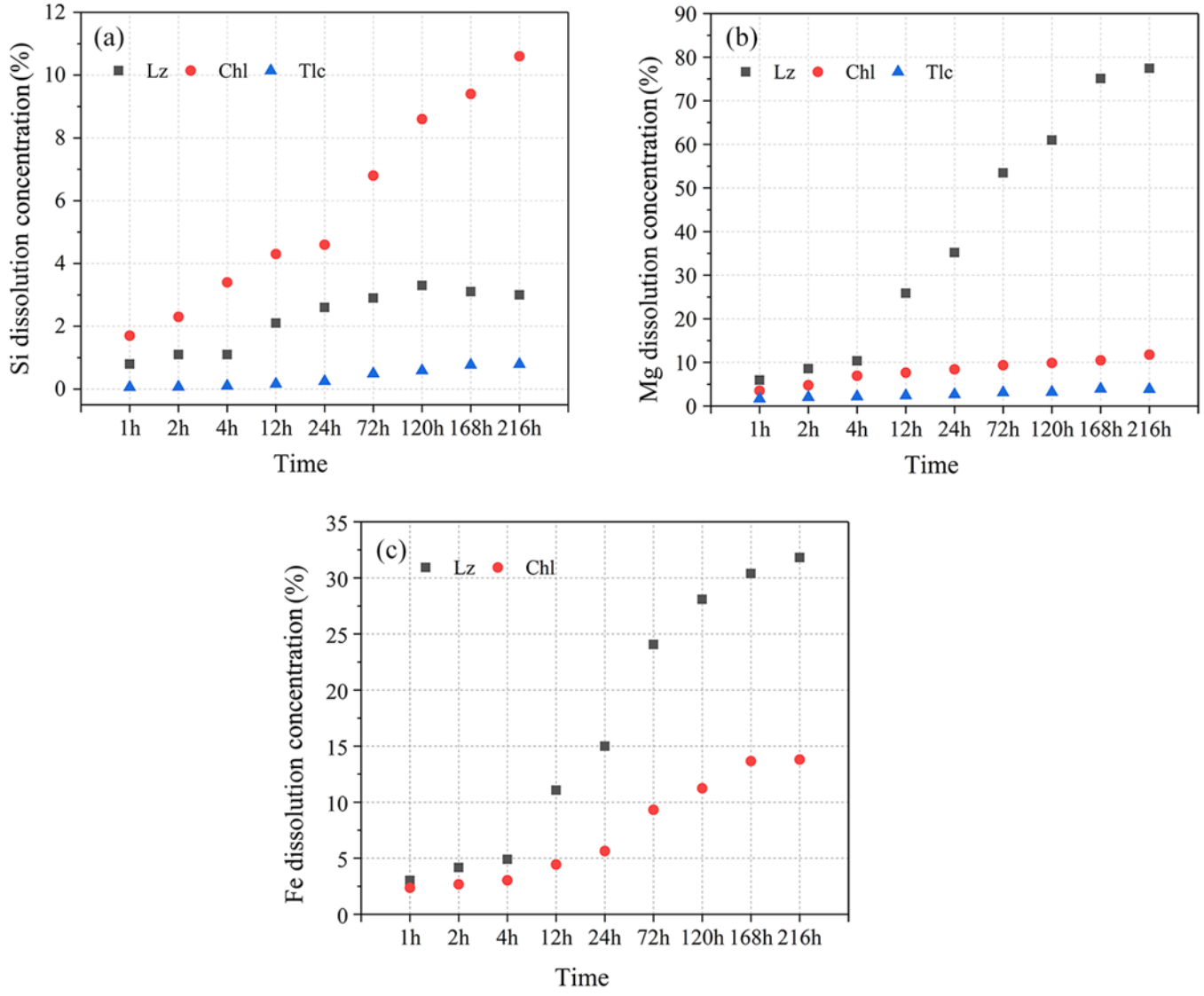

Figure 2. The relationships between (a) Si, (b) Mg and (c) Fe dissolution concentrations of lizardite (Lz), chlorite (Chl) and talc (Tlc) in sulfuric acid solution with reaction time.

Table 3. Al elemental analysis of the chlorite samples.

	Chl–1h	Chl–2h	Chl–4h	Chl–12h	Chl–24h	Chl–72h	Chl–120h	Chl–168h	Chl–216h
Al (mg L^{-1})	34.22	40.28	52.38	59.30	67.90	98.70	127.98	132.66	148.09
Al/Si	1.68	1.44	1.26	1.14	1.23	1.20	1.22	1.17	1.30

surface area is limited to certain crystal faces or is mainly controlled by surface defects (Nagy, 1995). This work uses the BET surface area as the mineral–water interfacial reaction surface area. The measured BET specific surface areas were found to be 17.8, 4.2 and 3.5 $m^2\ g^{-1}$ for lizardite, chlorite and talc, respectively. The specific surface area of lizardite is large (Lacinska *et al.*, 2016), so the dissolution rates of Si and Fe are lower than those of chlorite after normalization (Fig. 3a,c). After 24 h of the mineral–water interfacial reaction, the lizardite dissolution rate of Mg was higher than those of chlorite and talc (Fig. 3b). With the progress of the talc–water interfacial reaction, Mg on the edge (end face) of the talc gradually dissolves. Furthermore, the difficulty of H^+ attacking the $(OH)^-$ on the octahedral sheet gradually increases. Therefore, the dissolution rate of Mg in the talc is lower than those of lizardite and chlorite after 12 h. During the mineral–water interfacial reaction, the dissolution rates of Si and Mg of chlorite were found to be always greater than those of talc. Furthermore, in the tetrahedral sheet, Al replaces Si; thus, Al occupies ∼35% of the tetrahedral sheet. When chlorite reacts with the sulfuric acid solution, Al on the tetrahedral sheet dissolves before Si, resulting in defect sites on the tetrahedral sheet. Then, H^+ enters the mineral from these defect sites and reacts with the octahedral sheet, speeding up the dissolution rate of Mg (Rozalen *et al.*, 2014). This also causes the Mg dissolution concentration of chlorite to be greater than that of talc. During the lizardite–water interfacial reaction, the dissolution rate of Mg in lizardite consistently exceeds that of Fe. Within the

https://doi.org/10.1180/clm.2024.19 Published online by Cambridge University Press

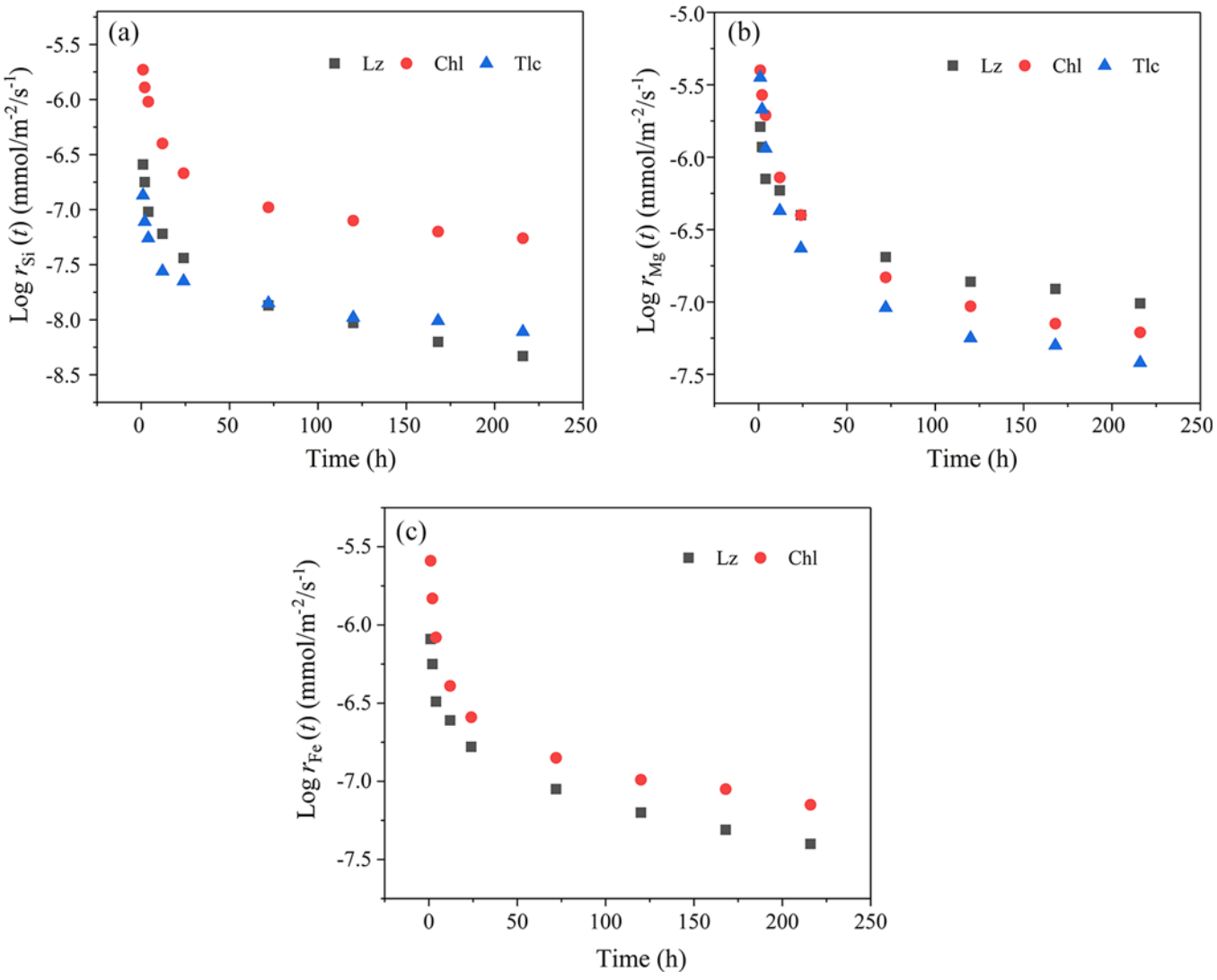

Figure 3. (a) Si, (b) Mg and (c) Fe (c) dissolution rates of lizardite (Lz), chlorite (Chl) and talc (Tlc) in sulfuric acid solution.

initial 72 h period of the chlorite–water interfacial reaction, the dissolution rate of Mg in chlorite surpasses that of Fe. Subsequently, after 72 h, the dissolution rate of Mg in chlorite falls below that of Fe.

The relative release ratio (RRR) of the dissolved ions to describe the stoichiometry of alkali feldspar dissolution at various pH values is calculated according to Equation 2 (Holdren & Speyer, 1985):

$$\mathrm{RRR_{Al/Si}} = (\mathrm{Al/Si})_{\mathrm{solution}}/(\mathrm{Al/Si})_{\mathrm{solid}} \quad (2)$$

where $\mathrm{RRR_{Al/Si}}$ is the RRR of Al to Si, such that its value is 1 for congruent dissolution, <1 when Si is released preferentially and >1 when Al is released preferentially. In lizardite, chlorite and talc, Mg could preferentially dissolve. In chlorite, Al could preferentially dissolve from the silica tetrahedral sheet compared to Si. This result is verified by relevant studies in the literature (Jurinski & Rimstidt, 2001; Kalinowski & Schweda, 2007; Rozalen *et al.*, 2008; Bibi *et al.*, 2011). Then, the (Mg/Si) ionic dissolution concentration ratio of chlorite decreases slightly with increasing reaction time and gradually tends to the ratio of the stoichiometric coefficient, which is consistent with the literature (Hamer *et al.*, 2003). The (Mg/Si) ionic dissolution ratio of lizardite increases with increasing reaction time, indicating that the dissolution rate of Mg is consistently greater than that of Si during the mineral–water interfacial reaction (Fig. 4). At the initial stage of the reaction at the water interface, H^+ preferentially reacts with Mg–OH at the edge of the octahedral sheet structure, and the dissolution rate of Mg is higher than that of Si. With the progress of the reaction, H^+ further reacts with Mg–OH inside the octahedral sheet, slowing down the dissolution rate of Mg. Therefore, the (Mg/Si) ionic dissolution ratio of talc first increases and then decreases with increasing reaction time.

Structural changes in lizardite, chlorite and talc during the mineral–water interfacial reactions in sulfuric acid solution

The characteristic diffraction reflection intensity of lizardite decreases with increasing reaction time after the mineral–water interfacial reaction in sulfuric acid medium (Fig. 5a). The characteristic reflection strength of chlorite decreased in the first 12 h after the mineral–water interfacial reaction but did not change significantly during the reaction from 12 to 168 h

https://doi.org/10.1180/clm.2024.19 Published online by Cambridge University Press

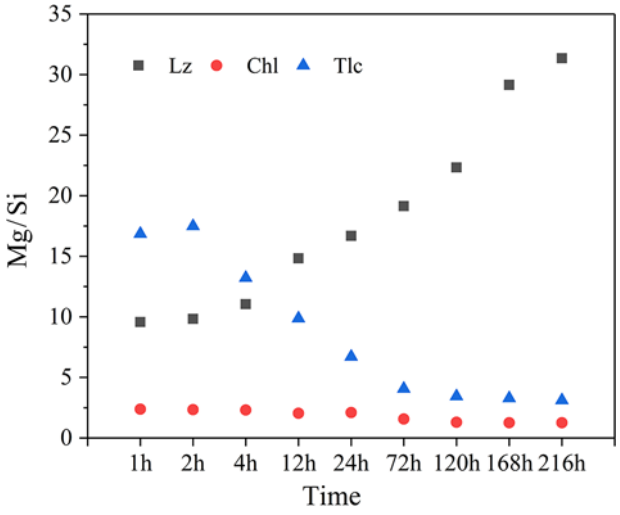

Figure 4. Changes in Mg/Si concentration ratios of lizardite (Lz), chlorite (Chl) and talc (Tlc) samples dissolved in sulfuric acid medium with reaction time.

(Fig. 5b). The reflection diffraction intensity, *Ic*(002)/*Ic*(001), of the characteristic reflection strength of chlorite can generally be used to calculate the degree of conversion to vermiculite (Weaver, 1956; Rich, 1968), such that the lower the ratio, the higher the degree of vermiculite. The strength ratio of *Ic*(002)/*Ic*(001) decreases after 72 h of reaction at the mineral–water interface, indicating that chlorite changes to vermiculite. The characteristic reflection intensity of talc hardly changed during the reaction (Fig. 5c).

The absorption reflections at 3690 and 3646 cm^{-1} are attributed to the stretching vibrations of the external and internal hydroxyl groups, respectively. Mg–O(H) has a characteristic reflection peak at 610 cm^{-1} (Chen *et al.*, 2023). The Si–O characteristic reflections at 1079 and 956 cm^{-1} are attributed to the stretching vibration of the Si–O bond perpendicular to the structural layer and the Si–O–Si bond parallel to the structural layer, respectively (Fig. 6a; Lacinska *et al.*, 2016; Beglaryan *et al.*, 2023). The intensity of each characteristic reflection gradually decreases with increasing reaction time. This indicates that Mg and Si in the mineral are gradually dissolved, the structure is destroyed and the amorphous SiO_2 structure is transformed. The gradual disappearance of the reflection at 610 cm^{-1} also confirms the dissolution of Mg in the lizardite structure (Liu *et al.*, 2022). The chlorite reflections show Si–O bending and stretching and Mg–O(H) bending absorptions in the 1300–500 cm^{-1} region (Meng *et al.*, 2018; Wang *et al.*, 2023). The bands at 987 cm^{-1} were attributed to the absorptions of Si–O–Si and Si–O–Al (Madejová, 2003). The band at 762 cm^{-1} was attributed to trioctahedral chlorite (Fig. 6b; Zhao & He, 2016). In the first 12 h after the reaction between chlorite and the sulfuric acid solution, the characteristic reflections of chlorite decrease with increasing reaction time. The characteristic reflection strength does not change significantly after the reaction at the water interface for 12 h. In talc, the stretching vibration reflection of Mg–OH at 3677 cm^{-1}, the Si–O stretching vibration reflection at 1018 cm^{-1} (Kubicki *et al.*, 1996; Madejová *et al.*, 1998) and the Si–O–Si bending mode at 669 cm^{-1} (Yang *et al.*, 2006; Nied *et al.*, 2016) did not change significantly during the mineral–water interfacial reaction with the sulfuric acid solution (Fig. 6c), which is consistent with the XRD data.

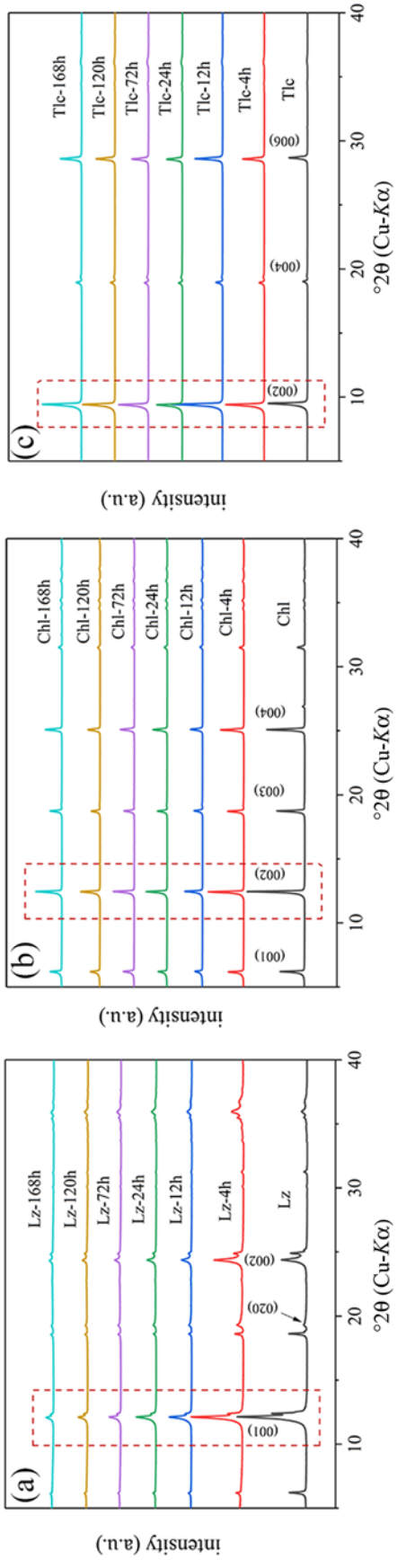

Figure 5. XRD traces of (a) lizardite (Lz), (b) chlorite (Chl) and (c) talc (Tlc) after various reaction times in sulfuric acid medium.

https://doi.org/10.1180/clm.2024.19 Published online by Cambridge University Press

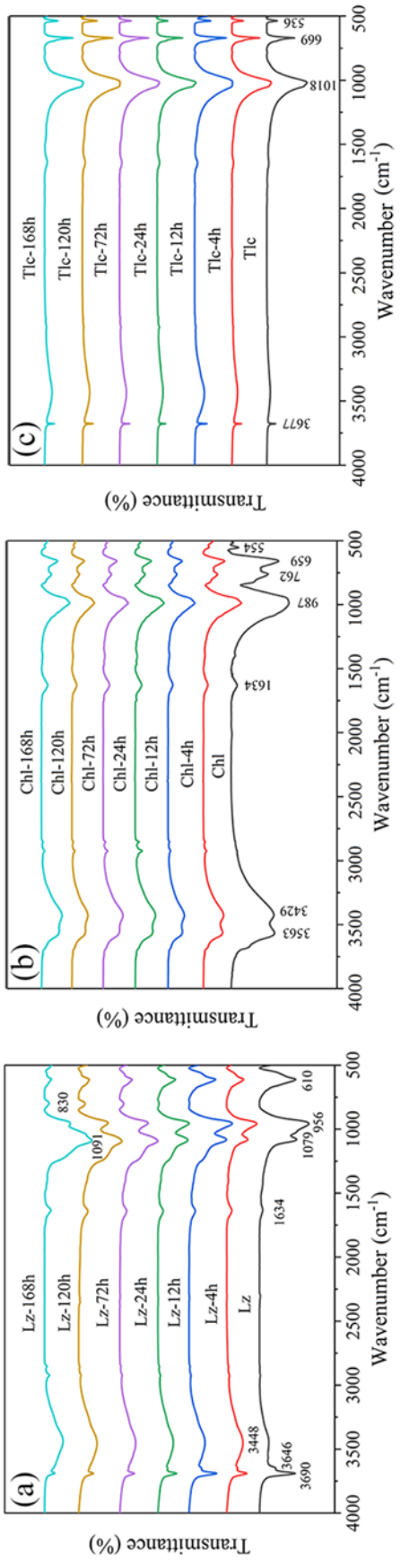

Figure 6. FTIR spectra of (a) lizardite (Lz), (b) chlorite (Chl) and (c) talc (Tlc) as raw samples and after various reaction times in sulfuric acid medium.

Micromorphological changes of lizardite, chlorite and talc during reaction in sulfuric acid solutions

The lizardite sample (Fig. 7a) mainly presents a lamellar micromorphology, with some small mineral particles and rod-like lizardite attached to the surface. After the mineral–water interfacial reaction between lizardite and sulfuric acid for 24 h (Fig. 7b), the laminar main structure is retained, the outer surface is corroded, the large layer structure is broken down into small layers and a small amount of amorphous silica is attached to the mineral surface. After 72 h (Fig. 7c), the lizardite was significantly corroded, and most layered structures became amorphous silica aggregates. With increasing reaction time, the surface of lizardite was gradually destroyed. Chlorite originally had a smooth surface and whole structure (Fig. 7d). After 24 h of reaction (Fig. 7e), the chlorite layer structure collapsed and the edge was destroyed. After 72 h (Fig. 7f), the extent of corrosion increased, and obvious structural defects appeared. The dissolution of chlorite in acidic solution occurred at the grain edge and at cracks and structural defects (Ross, 1969). For talc, after reaction for 24 h, the layered structure did not change significantly; the edge lamellae were attacked by H^+, the structure was destroyed and corroded and part of the structure of talc collapsed. After 72 h, the lamellae were smaller and were found to be adhered to the surface. Talc showed no obvious structural changes compared to those observed with lizardite and chlorite. Thus, the acid resistance of talc was stronger than that of lizardite and chlorite.

The lizardite layer was obvious (Fig. 8a), indicating greater crystallinity. After 24 h of reaction (Fig. 8b), lizardite showed fewer lattice stripes, indicating reduced crystallinity. For chlorite, after 24 h of reaction (Fig. 8d), the decrease in the interlayer space indicates that the crystal layer structure was damaged and the structural layer collapsed and compressed. This is consistent with the SEM results for chlorite (Fig. 7e,f). Talc shows lattice stripes and high crystallinity (Fig. 8e), and the interlayer space decreased after 24 h of reaction (Fig. 8f).

Mineral dissolution mechanism

The mineral–water interfacial reaction mechanisms of lizardite, chlorite and talc in acidic medium are summarized in Fig. 9. Lizardite has a TO layer structure with small particles. After H^+ from the acidic medium enters the interlayer domain, it can react with the $(OH)^-$ group on each octahedral sheet, and the Mg in the mineral structure can dissolve quickly. The Si–O bond in the tetrahedral sheet is stronger than the Mg–(O,OH) bonds in the octahedral sheet; thus, the dissolution concentration and dissolution rate of Si are smaller than those of Mg. The chlorite interlayer consists of (hydr)oxides, and the attack of H^+ on the octahedral sheet can be carried out through three pathways: (1) at the Mg–(OH) octahedral sheet in the interlayer sandwich, where some Mg is replaced by Al; (2) at the Mg–(O,OH) octahedral sheet in the middle of the TOT layer, where the reaction proceeds from the outside to the inside; and (3) at the defect site generated due to the substitution of Si by Al in the silicon tetrahedral sheet, then Al is preferentially dissolved, resulting in more structural defects. Therefore, the dissolution rates of Si and Mg in chlorite are consistently higher than those of talc during the mineral–water interfacial reaction. Talc contains a TOT layer, wherein H^+ enters the octahedral channel from the mineral edge and first reacts with Mg–OH at the edge, destroying the outer octahedral sheet and dissolving Mg. The talc–water interfacial reaction gradually occurred from the outside

https://doi.org/10.1180/clm.2024.19 Published online by Cambridge University Press

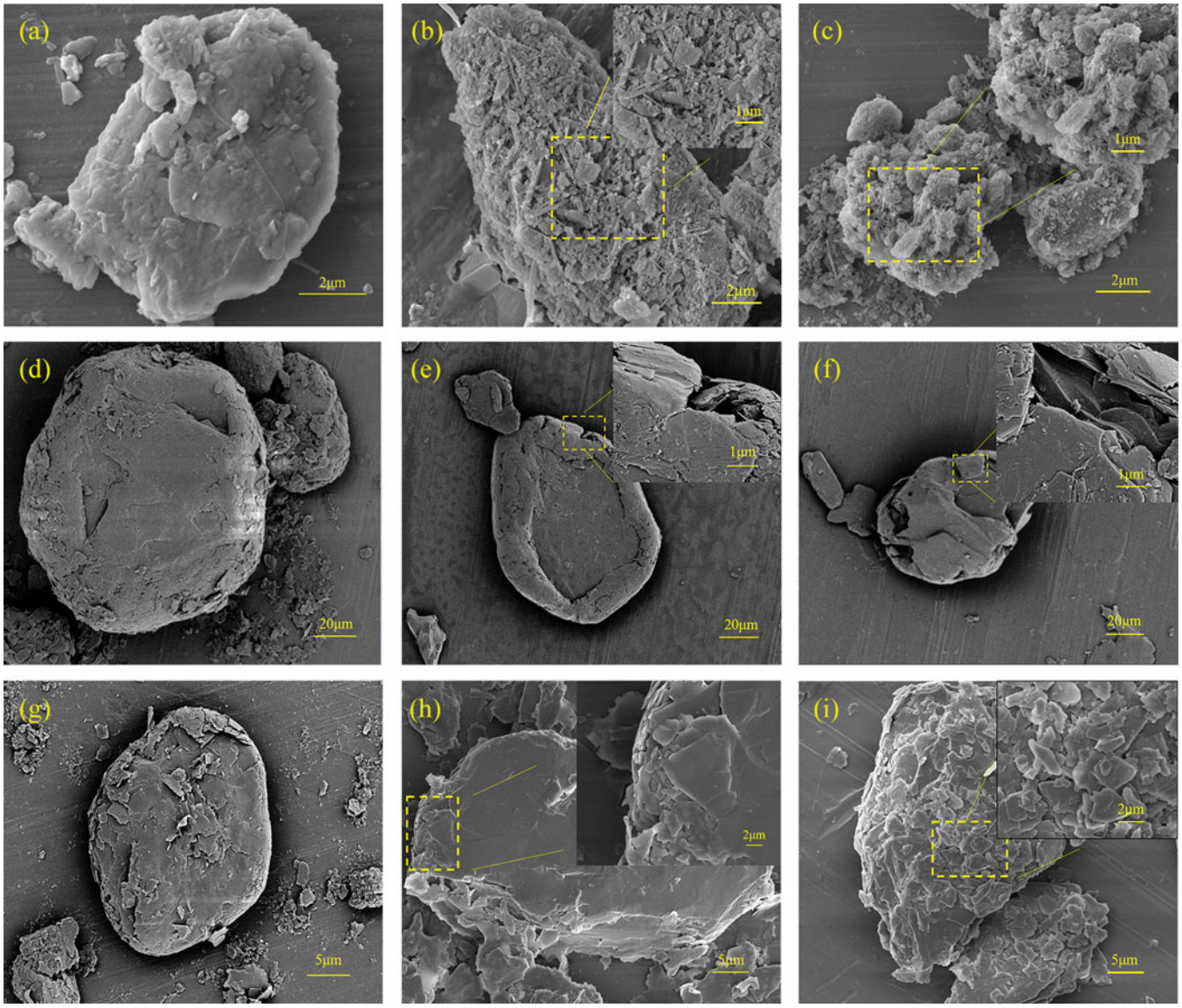

Figure 7. SEM images: (a) original lizardite sample, (b) lizardite in sulfuric acid for 24 h and (c) lizardite in sulfuric acid for 72 h; (d) original chlorite sample, (e) chlorite in sulfuric acid for 24 h and (f) chlorite in sulfuric acid for 72 h; and (g) original talc sample, (h) talc in sulfuric acid for 24 h and (i) talc in sulfuric acid for 72 h.

to the inside. As Mg is preferentially dissolved, the silica tetrahedral sheets on both sides gradually converge to the middle, blocking the reaction between H^+ and Mg–OH. Therefore, talc is the most stable mineral regarding the mineral–water interfacial reaction in an acidic medium.

Conclusions

The mineral–water interfacial reaction in acidic medium was studied with lizardite (TO type), talc (TOT type) and chlorite (TOT type, hydroxide interlayer). Different dissolution rates were obtained; the dissolution concentrations of Si in chlorite and Mg in lizardite were the highest, and the dissolution concentrations of Si and Mg in talc were the lowest. Furthermore, the dissolution rates of Si and Mg in chlorite were the highest, and the dissolution rate of Mg in lizardite was higher than that of talc at the later stages of the reaction. Thus, talc was found to be more stable than lizardite and chlorite in an acidic medium. The phase and structure of the minerals indicated that the structure of lizardite was gradually destroyed with increasing reaction time, as the ionic components of the three minerals dissolved. At the initial stage of the reaction, the structural damage to chlorite was obvious. The structure of talc did not change significantly over the course of the entire reaction. The microtopography of the minerals showed that the structural failure process of lizardite occurred from the outside to the inside. In the process of the structural failure of chlorite, the layered structure collapsed and many structural defects occurred. The surface layer of talc could be decomposed by corrosion into small lamellae structures attached to the surface, whereas there were no obvious structural changes in the lizardite and chlorite.

https://doi.org/10.1180/clm.2024.19 Published online by Cambridge University Press

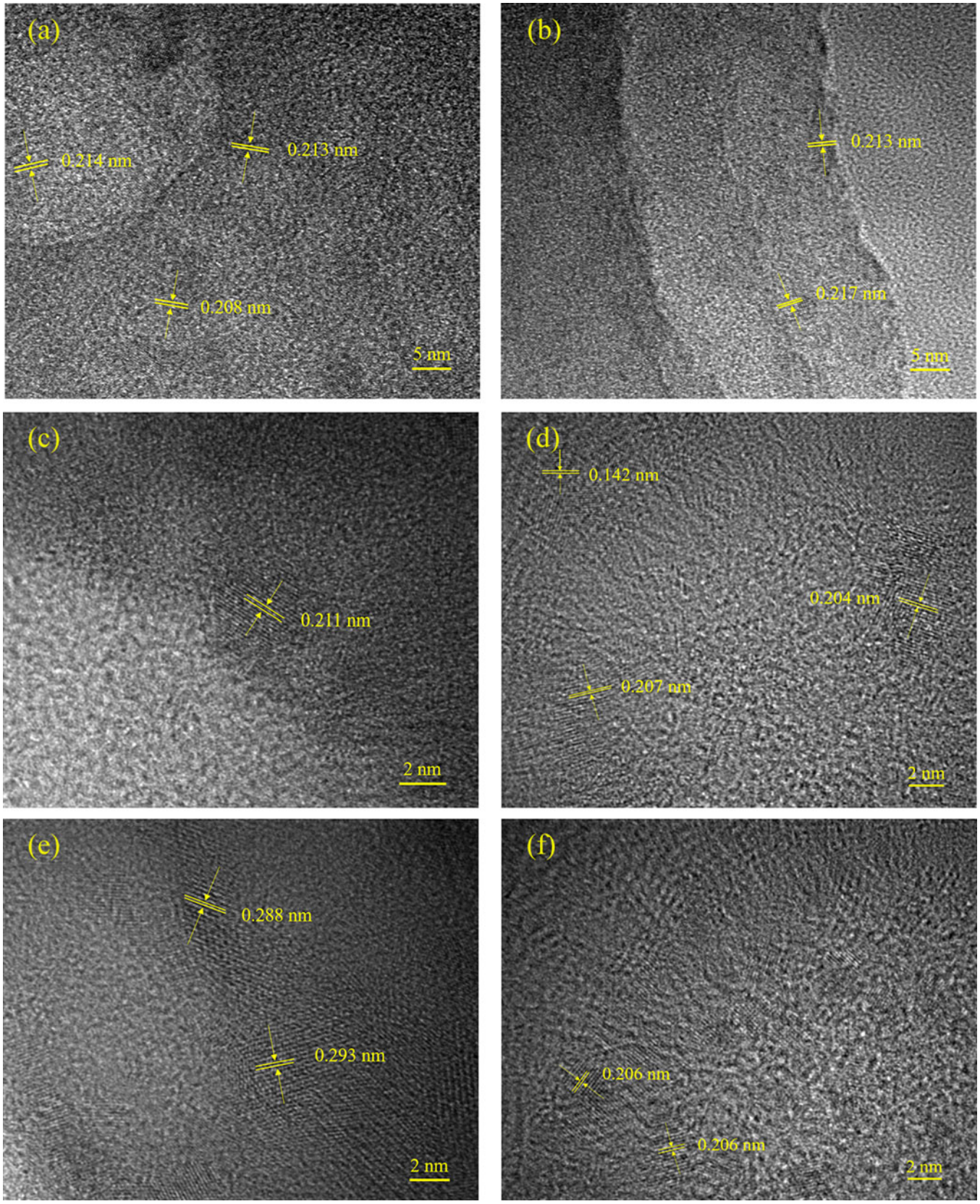

Figure 8. TEM images: (a) original lizardite sample and (b) lizardite in sulfuric acid for 24 h; (c) original chlorite sample and (d) chlorite in sulfuric acid for 24 h; and (e) original talc sample and (f) talc in sulfuric acid for 24 h.

https://doi.org/10.1180/clm.2024.19 Published online by Cambridge University Press

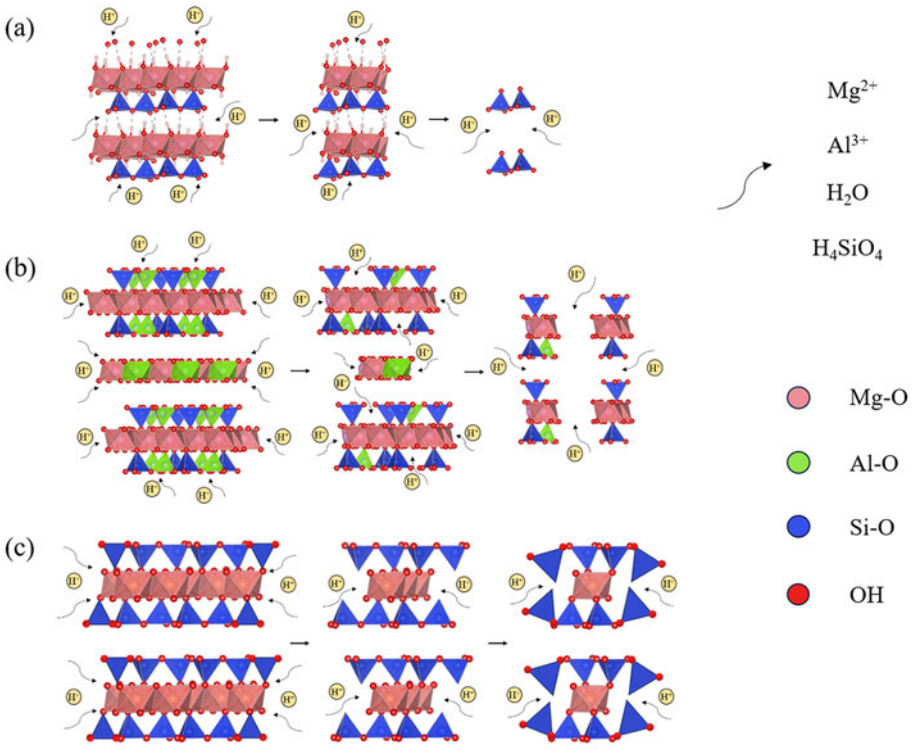

Figure 9. Schematic diagram of the mineral structures attacked by H^+: (a) lizardite, (b) chlorite and (c) talc.

Authors contributions. DZ: Writing – original draft, Visualization, Software, Data curation. HS and TP: Writing – review & editing, Validation, Supervision, Resources, Funding acquisition, Conceptualization. LZ and MW: Software, Methodology, Investigation.

Financial support. This study was supported by the National Natural Science Foundation of China (Grant No. 42072048).

Competing interests. The authors declare that they have no known competing financial interests or personal relationships that could have appeared to influence the work reported in this paper.

Data availability statement. Data will be made available on request.

References

Barnhisel R.I. & Bertsch P.M. (1989) Chlorites and hydroxy interlayered vermiculite and smectite. Pp. 729–788 in: *Minerals in Soil Environments* (J. Dixon & S. Weed, editors). Soil Science Society of America, Madison, WI, USA.

Beglaryan H., Isahakyan A., Zulumyan N., Melikyan S. & Terzyan A. (2023) A study of magnesium dissolution from serpentinites composed of different serpentine group minerals. *Minerals Engineering*, **201**, 108171.

Bibi I., Singh B. & Silvester E. (2011) Dissolution of illite in saline-acidic solutions at 25 °C. *Geochimica et Cosmochimica Acta*, **75**, 3237–3249.

Bo F., Lu Y. & Feng Q. (2013) Mechanisms of surface charge development of serpentine mineral. *Transactions of Nonferrous Metals Society of China*, **23**, 1123–1128.

Brigatti M.F., Galan E. & Theng B.K.G. (2013) Structure and mineralogy of clay minerals. *Developments in Clay Science*, **5**, 21–81.

Caruso L.J. & Chernosky J.V. (1979) The stability of lizardite. *Canadian Mineralogist*, **17**, 757–769.

Chen M., Wang C., Shi Q., Hu H., Zhang Q. & Li Z. (2023) Enhanced simultaneous CO_2 mineralization and cadmium immobilization in a wide pH range by using ball-milled serpentine. *Chemical Engineering Journal*, **474**, 145558.

Cuadros J., & Dudek T. (2006) FTIR investigation of the evolution of the octahedral sheet of kaolinite–smectite with progressive kaolinization. *Clays and Clay Minerals*, **54**, 1–11.

Evans B.W., Hattori K. & Baronnet A. (2013) Serpentinite: what, why, where? *Elements*, **9**, 99–106.

Fuchs Y., Linares J. & Mellini M. (1998) Mossbauer and infrared spectrometry of lizardite-*1T* from Monte Fico, Elba. *Physics and Chemistry of Minerals*, **26**, 111–115.

Galí S., Soler J.M., Proenza J.A., Lewis J.F., Cama J. & Tauler E. (2012) Ni enrichment and stability of Al-free garnierite solid-solutions: a thermodynamic approach. *Clays and Clay Minerals*, **60**, 121–135.

Ganor J., Mogollon J.L. & Lasaga A.C. (1999) Kinetics of gibbsite dissolution under low ionic strength conditions. *Geochimica et Cosmochimica Acta*, **63**, 1635–1651.

Gao J., Li X., Cheng G., Luo H. & Zhu H. (2023) Structural evolution and characterization of organic-rich shale from macroscopic to microscopic resolution: the significance of tectonic activity. *Advances in Geo-Energy Research*, **10**, 84–90.

Gazze S.A., Stack A.G., Ragnarsdottir K.V. & Mcmaster T.J. (2014) Chlorite topography and dissolution of the interlayer studied with atomic force microscopy. *American Mineralogist*, **99**, 128–138.

Grobéty B. (2003) Polytypes and higher-order structures of antigorite: a TEM study. *American Mineralogist*, **88**, 27–36.

Hamer M., Graham R.C., Amrhein C. & Bozhilov K.N. (2003) Dissolution of ripidolite (Mg, Fe-chlorite) in organic and inorganic acid solutions. *Soil Science Society of America Journal*, **67**, 654–661.

Hao W., Flynn L.S., Kashiwabara T., Alam M.S., Bandara S., Swaren L. *et al.* (2019) The impact of ionic strength on the proton reactivity of clay minerals. *Chemical Geology*, **529**, 119294.

He H., Cao J. & Duan N. (2019) Defects and their behaviors in mineral dissolution under water environment: a review. *Science of the Total Environment*, **651**, 2208–2217.

He H., Guo J., Xie X., Lin H. & Li L. (2002) A microstructural study of acid-activated montmorillonite from Choushan, China. *Clay Minerals*, **37**, 337–344.

https://doi.org/10.1180/clm.2024.19 Published online by Cambridge University Press

He Z.Y., Zhang Z.Y., Yu J.X., Xu Z.G. & Chi R.A. (2016) Process optimization of rare earth and aluminum leaching from weathered crust elution-deposited rare earth ore with compound ammonium salts. *Rare Earths*, **34**, 413–419.

Hegyesi N., Pongráccz S., Vad R.T. & Pukánszky B. (2020) Coupling of PMMA to the surface of a layered silicate by intercalative polymerization: processes, structure and properties. *Colloids and Surfaces A: Physicochemical and Engineering Aspects*, **601**, 12497.

Heller-Kallai L. & Rozenson I. (1981) Mössbauer studies of palygorskite and some aspects of palygorskite mineralogy. *Clays and Clay Minerals*, **29**, 226–232.

Holdren G.R. & Speyer P.M. (1985) pH dependent changes in the rates and stoichiometry of dissolution of an alkali feldspar at room temperature. *American Journal of Science*, **285**, 994–1026.

Jurinski J.B. & Rimstidt J.D. (2001) Biodurability of talc. *American Mineralogist*, **86**, 392–399.

Kalinowski B.E. & Schweda P. (2007) Rates and nonstoichiometry of vermiculite dissolution at 22°C. *Geoderma*, **142**, 197–209.

Knauss K.G. & Wolery T.J. (1988) The dissolution kinetics of quartz as a function of pH and time at 70 °C. *Geochimica et Cosmochimica Acta*, **52**, 43–53.

Kubicki J.D., Blake G.A. & Apitz S.E. (1996) *Ab initio* calculations on aluminosilicate Q^3 species: implications for atomic structures of mineral surfaces and dissolution mechanisms of feldspars. *American Mineralogist*, **81**, 789–799.

Lacinska A.M., Styles M.T., Bateman K., Wagner D., Hall M.R., Gowing C. & Paul D.B. (2016) Acid-dissolution of antigorite, chrysotile and lizardite for *ex situ* carbon capture and storage by mineralization. *Chemical Geology*, **437**, 153–169.

Li R., Yang C., Ke D. & Liu C. (2020) The scaling of mineral dissolution rates under complex flow condition. *Geochimica et Cosmochimica Acta*, **274**, 63–78.

Liao R., Chen W., Wang N. & Zhang J. (2021) Combined effects of temperature, mineral type, and surface roughness on chlorite dissolution kinetics in the acidic pH. *Applied Clay Science*, **201**, 105931.

Liu W., Peng X., Liu W., Zhang N. & Wang X. (2022) A cost-effective approach to recycle serpentine tailings: Destruction of stable layered structure and solvent displacement crystallization. *International Journal of Mining Science and Technology*, **32**, 595–603.

Madejová J. (2003) FTIR techniques in clay mineral studies. *Vibrational Spectroscopy*, **31**, 1–10.

Madejová J., Bujdák J., Janek M. & Komadel P. (1998) Comparative FTIR study of structural modifications during acid treatment of dioctahedral smectites and hectorite. *Spectrochimica Acta Part A: Molecular and Biomolecular Spectroscopy*, **54**, 1397–1406.

Mellini M. (1982) The crystal structure of lizardite *1T*: hydrogen bonds and polytypism. *American Mineralogist*, **67**, 587–598.

Mellini M. & Zanazzi P.F. (1987) Crystal structures of lizardite *1T* and lizardite-*2H1* from Coli, Italy. *American Mineralogist*, **72**, 943–948.

Meng J., Liu X., Li B., Zhang J., Hu D., Chen J. & Shi W. (2018) Conversion reactions from dioctahedral smectite to trioctahedral chlorite and their structural simulations. *Applied Clay Science*, **158**, 252–263.

Nagy K.L. (1995) Dissolution and precipitation kinetics of sheet silicates. *Reviews in Mineralogy and Geochemistry*, **31**, 173–233.

Nied D., Enemark-Rasmussen K., L'Hopital E., Skibsted J. & Lothenbach B. (2016) Properties of magnesium silicate hydrates (MSH). *Cement and Concrete Research*, **79**, 323–332.

Okada K., Temuujin J., Kameshima Y. & Kenneth J.D. Mackenzie. (2003) Selective acid leaching of talc. *Clay Science*, **12**, 159–165.

Palacios-Lidon E., Grauby O., Henry C., Astier J.P., Barth C. & Baronnet A. (2010) TEM-assisted dynamic scanning force microscope imaging of (001) antigorite: surfaces and steps on a modulated silicate. *American Mineralogist*, **95**, 673–685.

Palmieri F., Estoppey A., House G.L., Lohberger A., Bindschedler S., Chain P.S.G. & Junier P. (2019) Oxalic acid, a molecule at the crossroads of bacterial–fungal interaction. *Advances in Applied Microbiology*, **106**, 49–77.

Perez Rodriguez J.L., Maqueda C. & Justo A. (1985) Pyrophyllite determination in mineral mixture. *Clays and Clay Minerals*, **33**, 563–566.

Ren Y., Cao X., Wu P. & Li L. (2023) Experimental insights into the formation of secondary minerals in acid mine drainage-polluted karst rivers and their effects on element migration. *Science of the Total Environment*, **858**, 160076.

Rich C.I. (1968) Hydroxy interlayers in expansible layer silicates. *Clays and Clay Minerals*, **16**, 15–30.

Ross G.J. (1969) Acid dissolution of chlorites: release of magnesium, iron and aluminum and mode of acid attack. *Clays and Clay Mineral*, **17**, 347–354.

Rozalen M., Huertas F.J., Brady P.V., Cama J., Garcia-Palma S. & Linares J. (2008) Experimental study of the effect of pH on the kinetics of montmorillonite dissolution at 25 °C. *Geochimica et Cosmochimica Acta*, **72**, 4224–4253.

Rozalen M., Ramos M.E., Gervilla F., Kerestedjian T., Fiore S. & Huertas F.J. (2014) Dissolution study of tremolite and anthophyllite: pH effect on the reaction kinetics. *Applied Geochemistry*, **49**, 46–56.

Ruiz-Agudo E. & Putnis C.V. (2012) Direct observations of mineral fluid reactions using atomic force microscopy: the specific example of calcite. *Mineralogical Magazine*, **76**, 227–253.

Saldi G.D., Köhler S.J., Marty N. & Oelkers E.H. (2007) Dissolution rates of talc as a function of solution composition, pH and temperature. *Geochimica et Cosmochimica Acta*, **71**, 3446–3457.

Su H. & Zhou W. (2019) Mechanism of accelerated dissolution of mineral crystals by cavitation erosion. *Acta Geochimica*, **39**, 11–42.

Temuujin J., Okada K., Jadambaa T., MacKenzie K.J.D. & Amarsanaa J. (2003) Effect of grinding on the leaching behaviour of pyrophyllite. *Journal of the European Ceramics Society*, **23**, 1277–1282.

Urosevic M., Rodriguez-Navarro C. & Putnis C.V. (2012) In situ nanoscale observations of the dissolution of {10–14} dolomite cleavage surfaces. *Geochimica et Cosmochimica Acta*, **80**, 1–13.

Villanova-de-Benavent C., Cama J., Soler J.M., Domènech C., Galí S. & Proenza J.A. (2022) Dissolution kinetics of garnierites from the Falcondo Ni-laterite deposit (Dominican Republic) under acidic conditions. *Applied Geochemistry*, **143**, 105357.

Viti C. & Mellini M. (1997) Contrasting chemical compositions in associated lizardite and chrysotile in veins from Elba, Italy. *European Journal of Mineralogy*, **9**, 585–596.

Wang R., Zhang H., Sun W. & Han H. (2023) The inhibiting effect of Pb-starch on chlorite flotation and its adsorption configuration based on DFT computation. *Applied Surface Science*, **610**, 155482.

Weaver C.E. (1956) The distribution and identification of mixed-layer clays in sedimentary rocks. *American Mineralogist*, **41**, 202–221.

Yang H., Du C., Hu Y., Yang W., Tang A. & Avvakumov E.G. (2006) Preparation of porous material from talc by mechanochemical treatment and subsequent leaching. *Applied Clay Science*, **31**, 290–297.

Zhao X.Y. & He D.B. (2016) *Clay Mineral and Application in Oil and Gas Exploration and Development*. Petroleum Industry Press, Beijing, China, pp. 49, 58–63, 92–107. [In Chinese]

Zhu H., Huang C., Ju Y., Bu H., Li X., Yang M. & Lu Y. (2021) Multiscale multi-dimensional characterization of clay-hosted pore networks of shale using FIBSEM, TEM, and X-ray micro-tomography: implications for methane storage and migration. *Applied Clay Science*, **213**, 106239.

Zhu H., Li S., Hu Z., Ju Y., Pan Y., Yang M. & Qian W. (2023) Microstructural observations of clay-hosted pores in black shales: implications for porosity preservation and petrophysical variability. *Clay Minerals*, **58**, 310–323.

https://doi.org/10.1180/clm.2024.19 Published online by Cambridge University Press